Supporting Information

Strategy for scalable comb block polyolefin synthesis. Efficient graft of isotactic polypropylene to a commercial broad molecular weight distribution, hyperbranched, ethylene methylacrylate copolymer.

Patrick Brant, Jiemin Lu, Maksim Shivokhin, Sergey Yakovlev, Shuhui Kang, Bethany Welke, Melissa Raney, Joseph Throckmorton, Jennifer Rapp, Hao Wang, and Dalia Yablon

Table of Contents

Section 1. Hydrogen and Carbon-13 NMR of EMA 2
Section 2. Synthesis of vinyl terminated isotactic polypropylene (vt-iPP) 4
Section 3. NMR spectra of vt-iPP, iPP-OH, and EMA-cb-iPP products 5
Section 4. GPC Comparisons for vt-iPP and iPPOH 13
Section 5. Synthesis of EMA-cb-iPP-16k-24 15
Section 6. Hydrogen and Carbon-13 NMR of blend of EMA and iPP-OH 15
Section 7. WAXS Analysis of EMA-cb-iPP Samples 17
Section 8. X-Ray Scattering Measurements of Blends 19
Section 9. AFM: Impact of temperature on EMA-cb-iPP morphology. 23

Deleted
Deleted
Deleted
Deleted
Deleted

Section 1. Hydrogen and Carbon-13 NMR of EMA

The ^{1}H and ^{13}C NMR spectra recorded for the EMA are shown in **Figure S1**. A quantitative summary assessed from ^{13}C NMR of the several branches present in the EMA is provided in Table S1. Also provided is an assessment of the microstructure or triad sequence populations involving methylacrylate. The MA punctuations are largely isolated.

Table S1. Branch structure and concentration in EMA

	Number Branches/1000 Carbon	
Branches :		
	Including $COOCH_3$	Backbone without $COOCH_3$
Methyl	1.56	1.69
Ethyl	2.37	2.56
1,3-Diethyl	1.61	1.74
Butyl	3.20	3.47
Amyl	55.58	60.18
Hexyl+	2.20	2.38
Modifier :		
Dimethyl	0.00	0.00
Ester Functionalities :		
$COOCH_3$ as EME	29.25	31.67
$COOCH_3$ as EMM	2.79	3.02
$COOCH_3$ as MMM	0.00	0.00
COOCH3 on quaternary	4.71	5.10
Wt % MA	20.94	
Mole % MA	7.94	

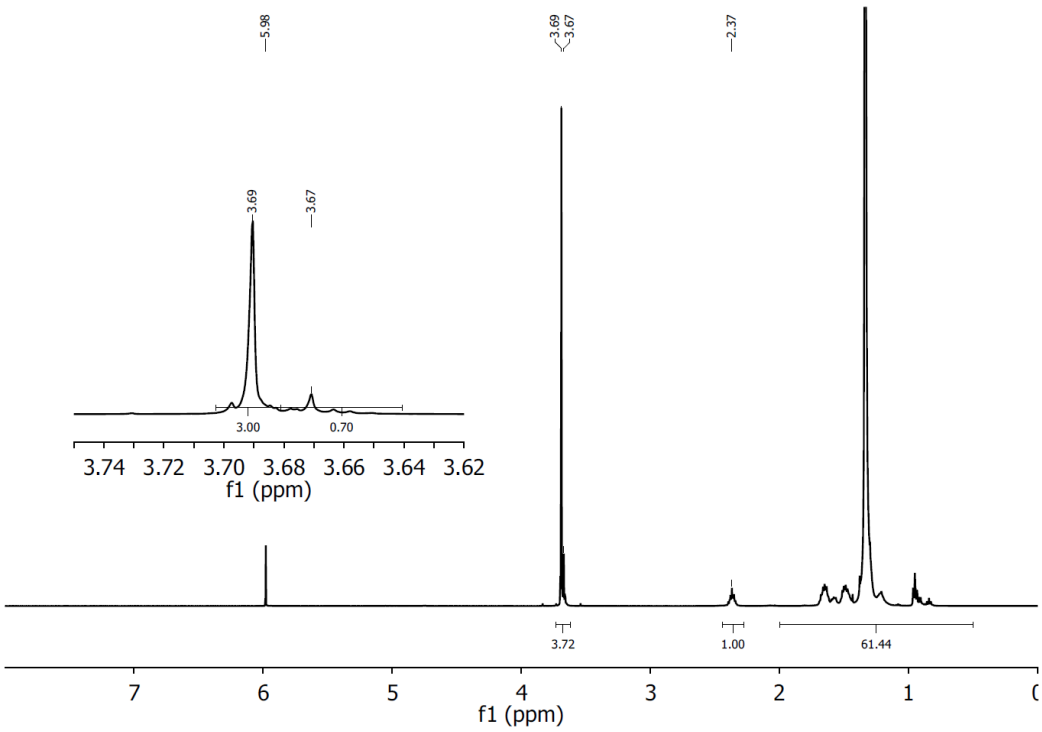
5.98
3.69
3.67
2.37
3.69
3.67
3.00
0.70
3.74 3.72 3.70 3.68 3.66 3.64 3.62
f1 (ppm)
3.72
1.00
61.44
7 6 5 4 3 2 1
f1 (ppm)

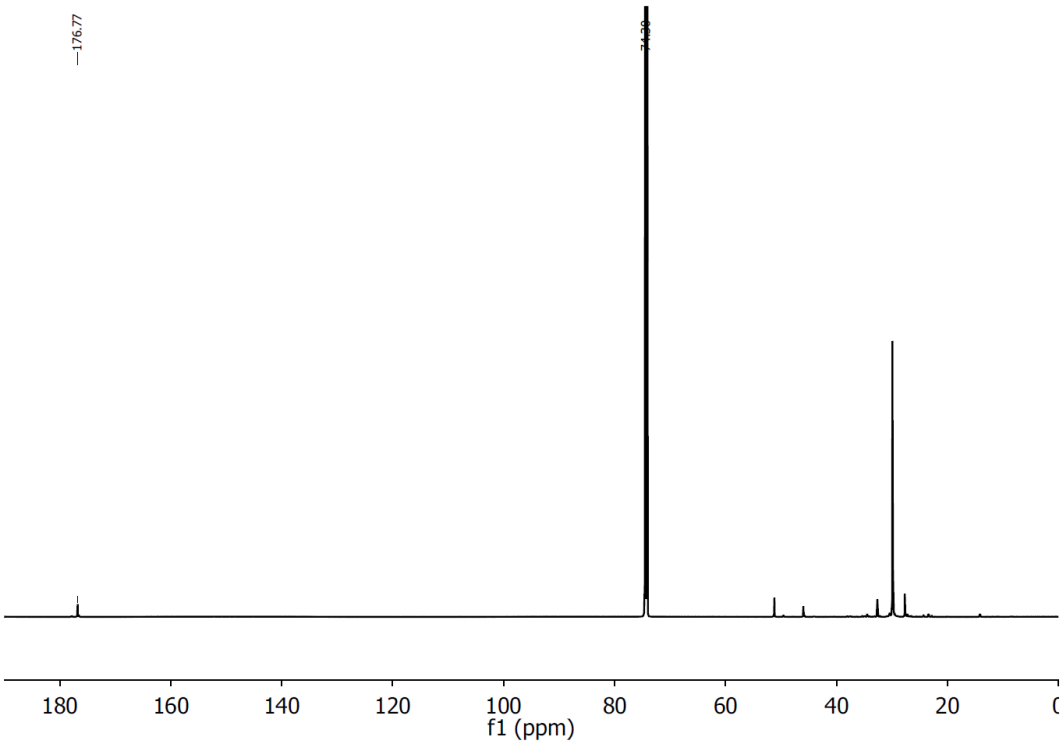
176.77
77.29
180 160 140 120 100 80 60 40 20
f1 (ppm)

Figure S1. Top: ^{1}H NMR (500 MHz, TCE-d_2, 120 °C) spectrum of EMA with inset shows the expanded region of 3.75-3.60 ppm. Bottom: ^{13}C NMR (600 MHz, TCE-d_2, 120 °C) spectrum of EMA.

Section 2. Synthesis of vinyl terminated isotactic polypropylene (vt-iPP)

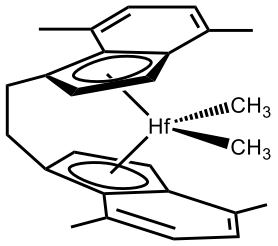

Synthesis was performed by propylene polymerization using rac-μ-ethylene bis(4, 7 dimethylindenyl)hafniumdimethyl (M1; structure shown above) activated with dimethylanilinium perfluorotetrakisnaphthenylborate (A1) (1:1.05 molar ratio dissolved in 3 ml toluene) in a 2l stainless steel autoclave reactor. Polymerization conditions, yield, and catalyst productivity are summarized in Table S2.

Table S2. Polymerization Conditions, vt-iPP made with **M1**-**A1**

Catalyst charge, mg	Propylene/hexanes charge*, mL	Temp, °C	Time, min	Productivity kg vt-iPP /g cat/hour
3.2	200/800	85	17	80

*0.5 ml 1 M Tri(isobutyl)aluminum scavenger added prior to catalyst addition

Section 3. NMR spectra of vt-iPP, iPP-OH, and EMA-*cb*-iPP products

In the course of this work, we have quantitatively characterized the topology and end groups in long chain branched polyolefins such as the vt-iPP and derivatives resulting from end group functionalization. The ^{1}H and ^{13}C NMR spectra for the vt-iPP, highlighting the resonances associated with the vinyl terminus, are shown in Figure S2. For vt LCB iPP and LCB iPPOH, the following equalities should apply.

For ^{13}C NMR (brackets are for molar concentrations):

$$[vinyl\ EG] + [LCB] = [isobutyl\ EG] \quad (1)$$

$$[vinyl\ EG]_{vt\ iPP} = [-CH_2OH]_{iPPOH} \quad (2)$$

$$[isobutyl\ EG]_{iPPOH} = [-CH_2OH]_{iPPOH} + [LCB]_{iPPOH} \quad (3)$$

Below, we examine NMR spectra in quantitative detail to provide the values to test equations (1), (2), and (3) above for ^{13}C NMR as well as equalities for ^{1}H NMR (equations (4) and (5)).

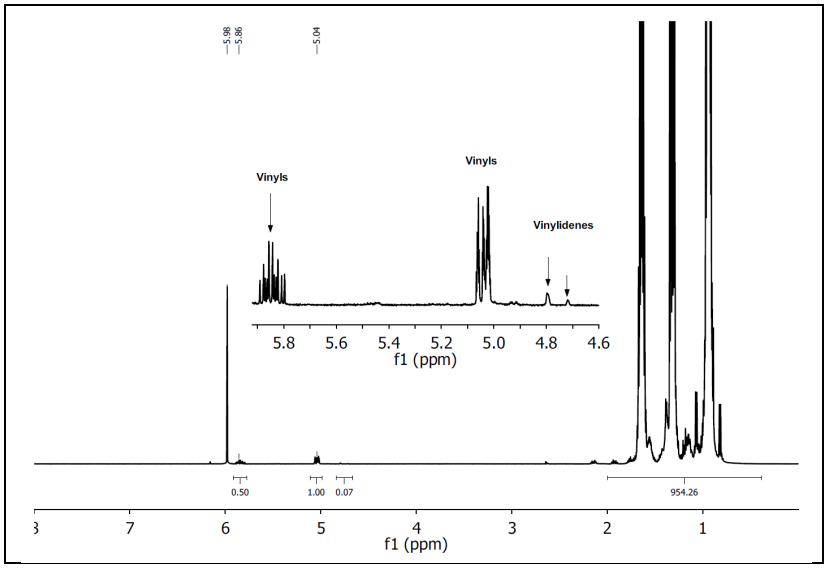

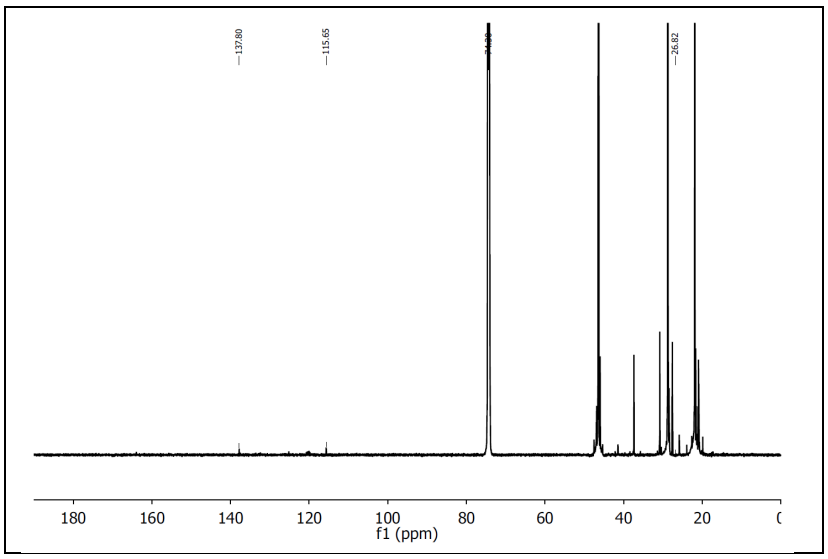

Figure S2. Top: ^{1}H NMR (500 MHz, TCE-d_2, 120 °C) spectrum of vt-iPP. Inset is the expanded region of 5.9-4.6 ppm showing the terminal vinyl resonances. Bottom: ^{13}C NMR (600 MHz, TCE-d_2, 120 °C) spectrum of vt-iPP showing the terminal vinyl resonances at 137.80 ppm and 115.65 ppm.

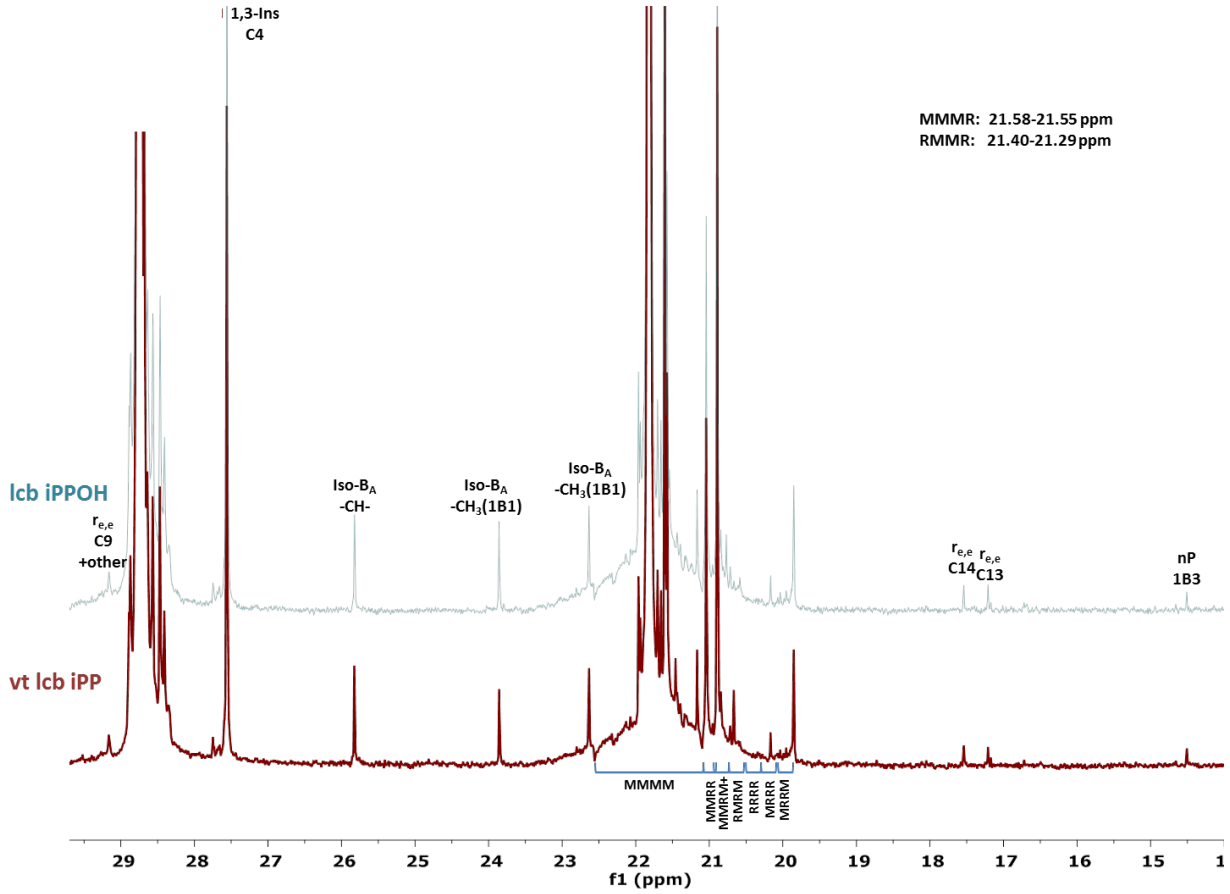

Figure S3. ^{13}C NMR comparison aliphatic region (14-30 ppm) vt LCB iPP (maroon) and LCB iPP-OH (teal) made with metallocene M1 activated with activator A1.

The 14-30 ppm region, which includes regio defects and saturated end groups (EG), is shown in Figure S3 for both LCB vt-iPP and LCB iPP-OH. The quantities of these defects are listed for each sample in Table S3. The isobutyl and n-propyl end groups are clearly observed in both spectra of LCB vt-iPP and LCB iPP-OH. The chemical shifts are 25.83, 23.87, 22.65 and 14.51 ppm, respectively.

The ^{1}H and ^{13}C NMR spectra for the vt-iPP are shown in Figures S1, S2, and S3. Olefinic unsaturations are the focus in Figures S1 and S2 while saturated end groups (isobutyl and n-propyl) and LCB are the focus in Figure S3. The ^{1}H NMR resonances for the -CH=CH_2 vinyl terminus iPP chain are centered at 5.86 ppm (-CH=) and 5.04 ppm (=CH_2 proton), respectively. These comprise 90 % of all unsaturations in the olefin region (but not 90 % of all the chains, as discussed in Experimental Section and detailed fully herein), with the remaining 10% associated with internal and terminal vinylidenes (~5:1 based on NMR). In Figure S2, the ^{13}C NMR shows the carbon resonances of the vinyl terminus at 137.80 ppm and 115.65 ppm representing the primary carbon and the secondary carbon respectively in -CH=CH_2 vinyl terminus.[5,6] The ratio of [vinyl/isobutyl] end groups is found to be 0.674 (Table 4). Resonances consistent with long chain branching are observed as well. Integration of these peaks reveals about 0.8 LCB/chain (number average basis). This vt-iPP also characteristically has high populations of stereo and regio defects, as can be seen in Figure S3, and consequently a lower iPP melting peak.

The calculated number average molecular weight (M_n) of this vt-iPP based on ^{1}H NMR is *ca.* 13,360, assuming one terminal vinyl (or vinylidene) group per chain while GPC-3D analysis gives a M_n of 15,262 and molecular weight distribution of ~2. The molecular weight distribution curve for the vt-iPP is shown in Figure **S6**. Consistent with the findings in ^{13}C NMR, the GPC-3D g′ value versus log M analysis (Figure **S7**) also indicates that this vt-iPP is moderately long chain branched. Branching is attributed to vt-iPP macromonomer re-insertion[6] during polymerization. The depression of g′ with molecular weight is consistent with this model. It is worth noting that the unique branch due to the macromonomer re-insertion has been identified by ^{13}C NMR in another LCB iPP made with this catalyst under similar conditions in the same reactor.

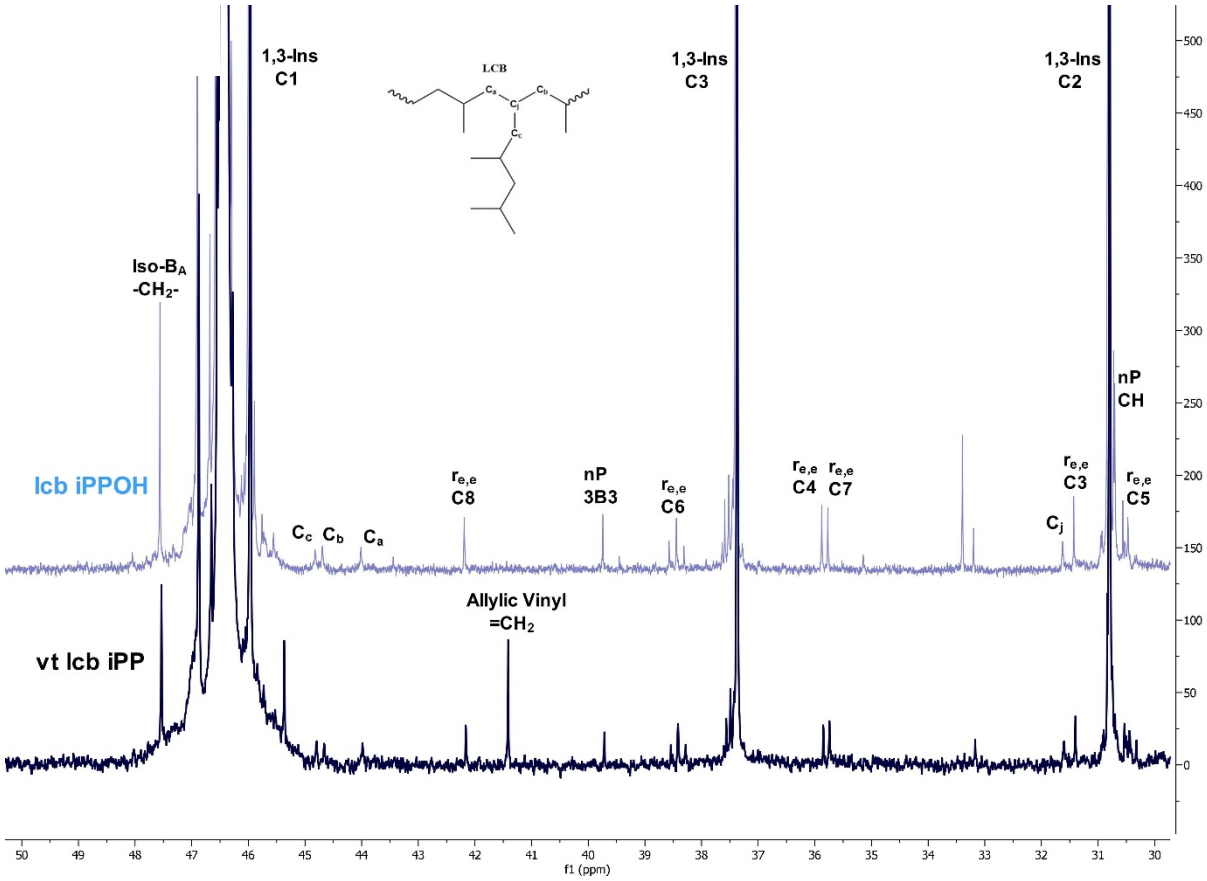

Figure S4. ^{13}C NMR 30-49 ppm region for LCB vt- iPP (maroon) and LCB iPP-OH (teal).

The region from 30-50 ppm (Figure S4) contains signals due to long chain branching (LCB). These are found in the spectra for both materials, and are clearly marked by the peaks at 44.80, 44.67, 43.99 and 31.58 ppm, labeled as C_c, C_b, C_a, and C_j, respectively in the figure. These assignments are based upon and consistent with the work done by Weng et. al.[6] The long chain branching concentrations measured for these samples are equal within experimental error, and are included in Table S3.

Finally, in Figure S5 we show the alcohol region of the ^{13}C NMR for both samples. Only the LCB iPP-OH shows an alcohol signal (63.67 ppm). The concentration of $–CH_2OH$ groups in the LCB iPP-OH is provided in Table S3 as well.

Table S3. Quantitation Summary of End Groups and long chain branches (LCB) from ^{13}C NMR

	Mol EG/mol $C_3^=$	
End Group/LCB	Vt-iPP	iPP-OH
mol vinyls	0.002(3) [0.0017][a]	0.000(0)
mol nP end groups	0.000(6)	0.000(5)
mol nB end groups	0.000(0)	0.000(0)
mol C-OH	0.000(0)	0.001(7)
mol Iso-Butyl-A groups	0.003(8)	0.003(7)
LCB per 10,000*	9	10

* not as reliable, due to increased error associated with method

Using both ^1H NMR and ^{13}C NMR, the quantification of key saturated and functional end groups as well as long chain branching has been achieved and the results are summarized in Table S4. With these data we can critically examine the outcomes relative to equations (1) through (5), re-stated below:

$$[vinyl\ EG] + [LCB] = [isobutyl\ EG] \quad (1)$$

$$[vinyl\ EG]_{vt\ iPP} = [-CH_2OH]_{iPPOH} \quad (2)$$

$$[isobutyl\ EG]_{iPPOH} = [-CH_2OH]_{iPPOH} + [LCB]_{iPPOH} \quad (3)$$

For ^{13}C NMR comparison with ^1H NMR:

$$HNMR\ [vinyl\ EG] = CNMR\ [vinyl\ EG] \quad (4)$$

$$HNMR\,[-CH_2OH]_{iPPOH} = CNMR\,[-CH_2OH]_{iPPOH} \quad (5)$$

The outcomes are organized in Table S5.

Table S4. Summary of Important End Group, Functional Group, and Long Chain Branching Concentrations Derived from ^{1}H and ^{13}C NMR

	/1000C									
	n-Pr EG		**Isobutyl EG**		**LCB**		**-CH_2-OH**		**Vinyl (allyl)**	
	^{1}H	^{13}C	^{1}H	^{13}C	^{1}H	^{13}C	^{1}H	^{13}C	^{1}H	^{13}C
LCB vt iPP	n.m.	0.6	n.m.	3.8	n.m.	0.9	0	0	1.64	1.7
LCB iPP-OH	n.m.	0.5	n.m.	3.7	n.m.	1.0	0.9	1.7	0.29	0.0

A comparison of measured data with the model, reflected in the equalities of equations (1)-(5), is provided in Table S5. We find the data fit well for equations 2 and 4 whereas there is significant disagreement in equations 1, 3, and 5. It is notable that the extent of enhancement of i-Bu EG relative to (*vinyl* + LCB) in equation (1) is the same, within experimental error, as its enhancement relative to (-OH + LCB) in equation (3). These two equations indicate an "excess" of i-Bu EGs is present in the products relative to the model embodied by these equations. Some enhancement of isobutyl chain ends may be due to 2,1 insertion of propylene into a M-H bond; and chain transfer to aluminum (scavenger) of a growing chain containing an i-Bu EG would result in a doubly saturated chain. In the case of equation (5) the inequality in –OH concentration measured by ^{1}H and ^{13}C NMR appears to be due to an "error" in the ^{1}H NMR measurement as the –OH concentration in LCB iPP-OH measured by ^{13}C NMR nearly equals the vinyl concentration measured in LCB vt iPP by both ^{1}H and ^{13}C NMR.

Table S5. Equality Comparisons; Measured versus Expected

Equation	Lhs	Rhs
(1) [(vinyl+LCB)/i-Bu]	2.6	3.8
(2) (vinyl/-OH)	1.7	1.7
(3) [i-Bu/(-OH+LCB)]	3.7	2.7
(4) [vinyl] (^{1}H vs ^{13}C NMR)	1.64	1.7
(5) [-OH] (^{1}H vs ^{13}C NMR)	0.9	1.7

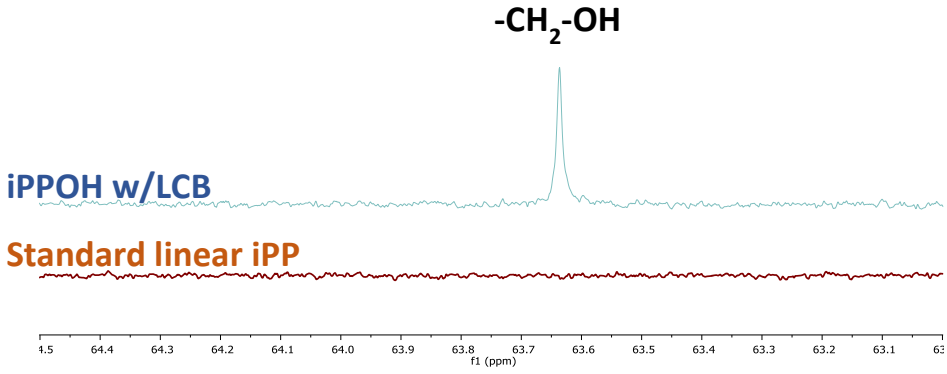

Figure S5. ^{13}C NMR of alcohol region for iPP-OH created by oxidative hydroboration of vt-iPP versus a standard linear iPP.

The assignments and integrals for peaks observed in the ^{1}H NMR of the EMA-*cb*-iPP products are organized in Table S6. These serve, with other measurements such as GPC-4D, to establish the grafting of iPP-OH to the EMA backbone.

Table S6. Integrations and structural assignments from ^{1}H NMR analyses in both EMA-*cb*-iPP products (EMA-*cb*-iPP-16k-24 and EMA-*cb*-iPP-16k-38) using ^{1}H NMR analysis.

Sample ID	Integrations of ^{1}H NMR resonances			
	MA COO***CH$_3$*** resonance *ca.* 3.69 ppm	iPP COO***CH$_2$***CH$_2$ resonance *ca.* 4.10 ppm	CH$_2$***CH*** resonance of MA/iPP and ethylene backbone joint *ca.*2.37 ppm	Total ***CH*** resonance *ca.* 2.0-0.5 ppm
EMA-*cb*-iPP-16k-24	3198	23.33	1000	92991
EMA-*cb*-iPP-16k-38	3193	46.24	1000	119431

Section 4. GPC Comparisons for vt-iPP and iPPOH

The chromatograms for vt-iPP and the iPP-OH synthesized from it are overlayed in Figure S6 while the branching index, g', for each as a function of Log M is compared in Figure S7. Ideally, the only difference between the two polymers is the end group (vinyl and an added hydroxyl accompanied by saturation of the vinyl), so we expect their GPC metrics to be very similar. These two comparisons show that, as expected the molecular weight and topology metrics for the iPP-OH closely match those for the vt-iPP from which it came. Moreover, these are in keeping with comparisons of the two – vt-iPP and iPP-OH – by other methods (DSC, ^{1}H and ^{13}C NMR) that also show a close match.

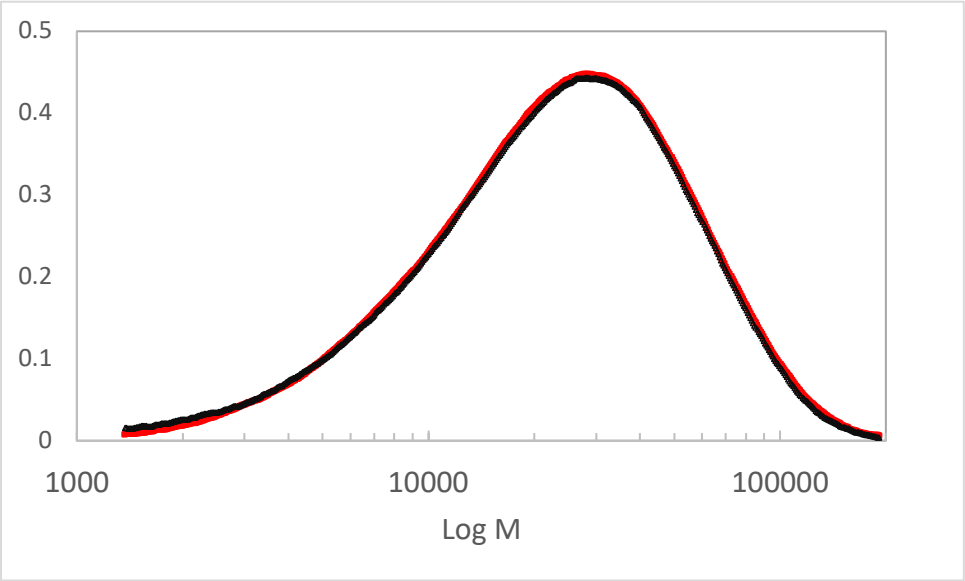

Figure S6. GPC DRI vt-iPP (black) and iPP-OH (orange).

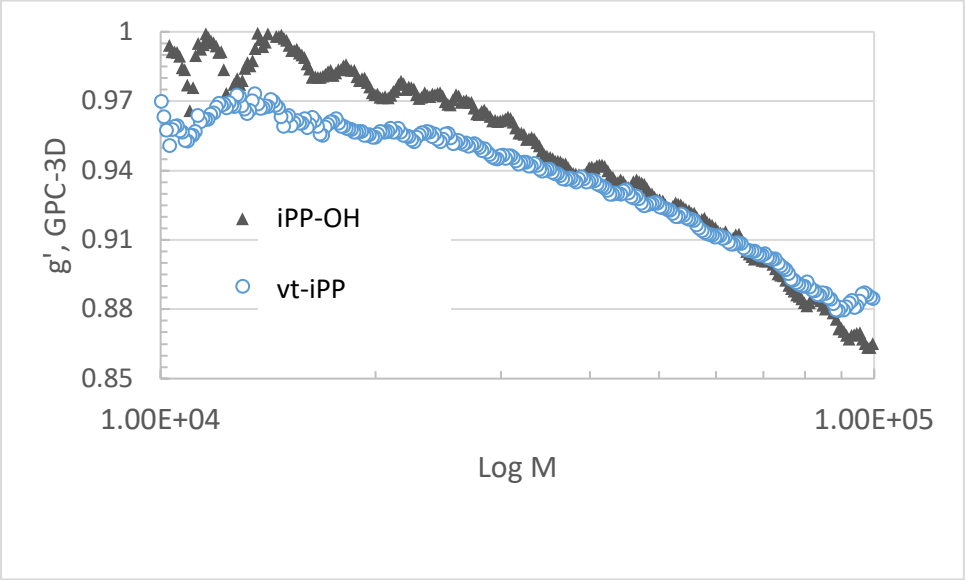

Figure S7. g′ GPC-3D comparison for vt-iPP (open blue circles; g'_{vis} = 0.85) and iPP-OH (black triangles; g'_{vis} = 0.83)

Section 5. Synthesis of EMA-*cb*-iPP-16k-24

Under dry nitrogen purge, EMA (3.00 g; 7.3 mmol MA), iPP-OH (1.5 g; 0.11 mmol hydroxyl functional group based on ^{1}H NMR), xylenes (100 mL) and *p*-toluenesulfonic acid (Aldrich, 45 mg) were added to a 250 mL single-neck round bottom flask equipped with a magnetic stir bar. The reaction mixture was refluxed at 205 °C for 20 h before it was poured into cold hexanes (500 mL). After the mixture cooled to room temperature, *n*-isopropanol was added and the resulting white powdery polymer was filtered and dried at 60-70 °C *in vacuo* for 24 h to afford a white product (4.0 g, 89 % yield).

Section 6. Hydrogen and Carbon-13 NMR of blend of EMA and iPP-OH

Hydrogen and carbon-13 NMR spectra were recorded for the physical blend of EMA and iPP-OH treated in the same dissolution, thermal and quench history as used to graft the iPP-OH to the EMA except in this instance no acid catalyst was employed. The spectra for the blend prepared in this way are provided in Figures S8 and S9. The spectra show that there is no ester resonance from the -C(O)-O-CH_2- linkage due to transesterification, while we find the undiminished alcohol resonance from the iPP-OH, detected at 63.68 ppm.

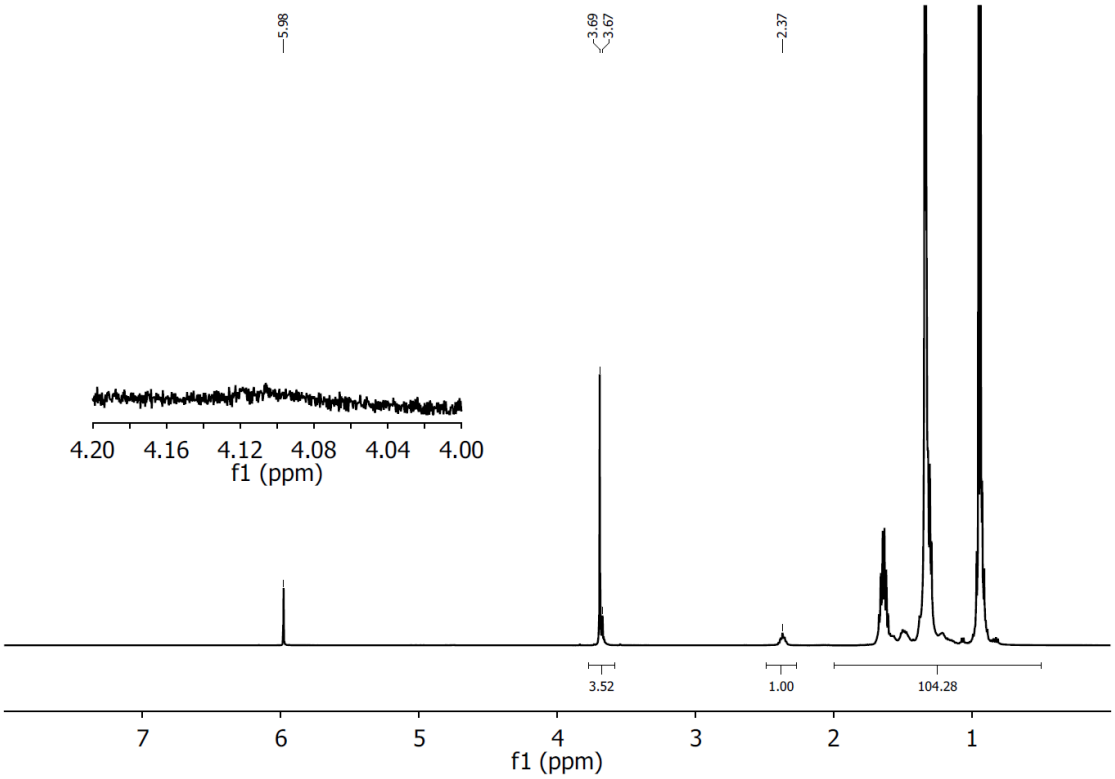

Figure S8. ^{1}H NMR (500 MHz, TCE-d_2, 120 °C) spectrum of physical blend of EMA and iPP-OH subjected to same conditions as used in comb block syntheses but without acid catalyst. Inset shows no significant resonance in the expanded region of 4.2-4.0 ppm and no evidence of transesterification.

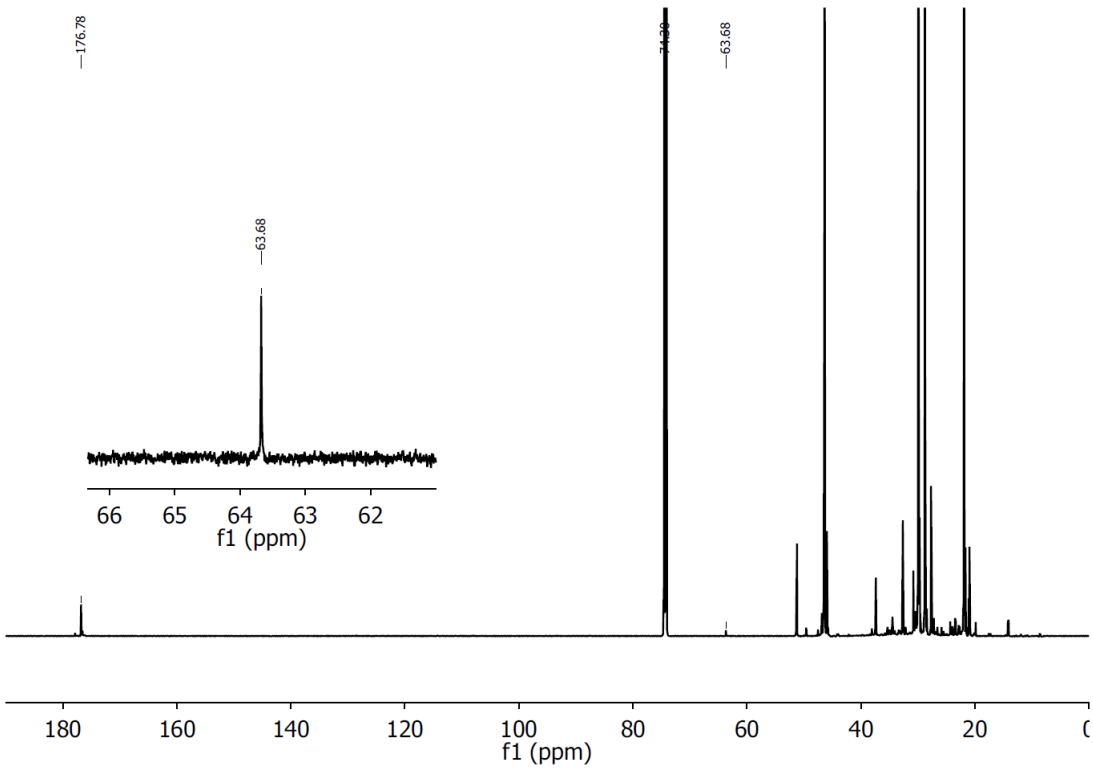

Figure S9. ^{13}C NMR (600 MHz, TCE-d_2, 120 °C) spectrum of isolated product from solution blend of iPP-OH and EMA exposed to same conditions and the grafting reactions except not acid was added. Inset shows only the resonance of iPP-OH detected at 63.68 ppm in the region of 62-66 ppm. No evidence of consumption of alcohol or transformation of methylacrylate groups.

Section 7. WAXS Analysis of EMA-cb-iPP Samples

The EMA and iPP crystallinities of the two EMA-cb-iPP comb block polymers were estimated from WAXS by deconvolution of the amorphous halos from both phases from the crystalline diffraction peaks. These estimated crystallinities, along with the iPP α, β, γ phase content, are summarized in Table S7.

Table S7. Estimation of PE and iPP crystallinities in EMA-*cb*-iPP samples from curve fitting WAXS 1D pattern

Sample	Crystallinity (%)			iPP Phase content (%)		
	Overall	EMA	iPP	α	β	γ
EMA-*cb*-iPP-16k-24	25.3	29.9	23.6	77.6	0.0	22.4
EMA-*cb*-iPP-16k-38	29.1	26.2	29.6	72.5	0.0	27.5

A sample of the pure EMA was used as a reference to model the amorphous halo from that phase and separate it from the iPP diffraction peaks. The crystalline content was calculated based on the integrated area of the amorphous to crystalline peak ratios.

$$\%\boldsymbol{crystallinity} = \frac{\boldsymbol{integrated\ area\ of\ crystalline\ peaks}}{\boldsymbol{total\ integrated\ area}}$$

The reported overall crystallinity values for both samples were estimated using the integrated area of all the crystalline diffraction peaks from the scattering pattern. The values for EMA and iPP crystallinity come from only peaks from those phases. The increase in overall crystallinity is coming from the increase in density of grafted iPP arms, allowing for larger iPP crystallite sizes and smaller EMA crystallite sizes. This can be seen from the changes in the full width at half maximum (FWHM) of the respective crystalline peaks for each phase. As the overall crystallinity increases, the EMA region crystallinity decreases, while the iPP region increases.

This is in agreement with the DSC data (Figure 5) when looking at the sizes of the endothermic peaks associated with the two regions melting behavior. However, the actual values calculated for the crystallinities differ. One explanation is that it could be attributed to the broadness of the DSC endothermic peak of the EMA melting event, making finding the area

difficult. Another probable answer would be the inherent difficulty in deconvolting the two separate amorphous halos in the WAXS fits. This is further complicated by the near overlap of the EMA primary diffraction peak with multiple iPP peaks. There is always some fitting parameter dependency, especially in blended materials, however care was taken to maintain the approximate positions for a relative comparison.

The iPP crystalline phase content was estimated using the relative peak heights of the 130α and 117γ reflections, which are unique to each respective phase. In the α/γ crystalline system:

$$G_{\gamma} = \frac{H_{\gamma}(117)}{H_{\gamma}(117) + H_{\alpha}(130)}$$

A possible reason for the presence of gamma crystals could be due to the restricted volume in which iPP has to crystallize given the block structures of these samples. This could lead to an increase in formation of the thermodynamically less stable gamma crystal.

Section 8. X-Ray Scattering Measurements of Blends.

Blends of EMA, iPP, and EMA-cb-iPP were also investigated with Wide- and Small-Angle X-Ray Scattering. Similar to the previous blends, the weights of components are included in the table below (**Table S8).**

Table S8. Blends investigated in the x-ray study

Sample	Weight %	
2 MFR iPP homopolymer; MP 164 ºC	40	38
EMA	60	58
EMA-*cb*-iPP-16k-38		4
Total	100	100

Figure S10 shows the addition of 4 wt% of EMA-*cb*-iPP-16k-38 acts to suppress the crystallinity and crystal size of pure EMA. Pure EMA crystallizes in an orthorhombic unit cell with small crystallite sizes as evidenced by the breadth of the FWHM of the diffraction peaks. Looking at the binary blend of EMA/iPP there is a convolution of scattering contribution from both EMA and iPP crystal domains. This is typical of a binary blend of phase separated materials. The two reflections at ~1.50 $Å^{-1}$ (111α) and ~1.55 $Å^{-1}$ ($13\bar{1}\alpha$ and 041α) from the alpha-phase iPP are split by the broad orthorhombic 110 reflection from EMA making peak deconvolution challenging. Upon addition of 4wt% EMA-*cb*-iPP-16k-38, the near disappearance of the EMA diffraction peaks implies significant reduction in EMA crystallinity and crystallite size. The AFM images of samples **B4** and **B5** help to confirm this assessment.

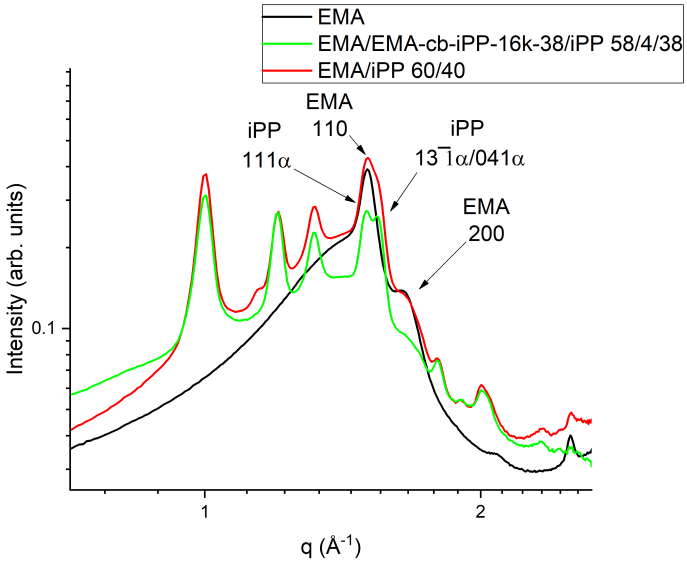

Figure S10. Upon addition of a small amount of comb block EMA-*cb*-iPP-16k-38, crystallinity and crystal size of the associated orthorhombic EMA diffraction peaks is suppressed. This implies a reduction in domain size as well as an support for compatibilization (observed by AFM and STEM).

SAXS shows a similar behavior in which the inter-lamellar spacing peak (Lp) appears to narrow upon addition of the compatibilizer (**Figure S11**). In the EMA/iPP blend, this peak consists of a convolution of long-range order peaks from both materials. When the comb-block material is added, a large portion of the EMA long-range order is destroyed. The SAXS pattern more closely resembles that of pure iPP, in which the second-order (002) lamellar diffraction peak is now clearly visible.

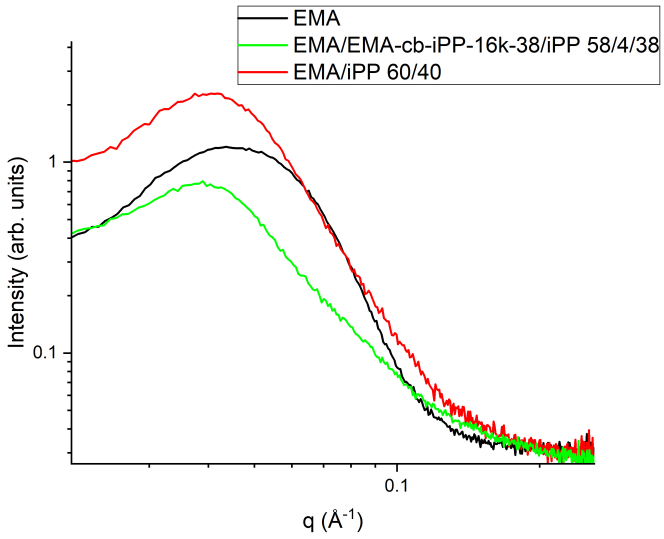

Figure S11. SAXS curves showing compatibilization of EMA and iPP by addition of 4 wt% EMA-*cb*-iPP-16k-38

Upon heating, the small crystals of EMA that remain in the ternary blend melt first and can be seen by the quick disappearance of the 200 diffraction peak in WAXS and the sharpening of the iPP inter-lamellar spacing peak in SAXS as well as observing the more well-defined 002 lamellar reflection (**Figure S12**). The iPP crystalline and inter-lamellar diffraction peaks persist at high temperatures. The swelling of the unit cell and average lamellar spacing can be observed by the shifting to lower q values of the corresponding diffraction peaks. As is typical with iPP, the primary expansion of the unit cell occurs along the crystallographic b-axis of the unit cell

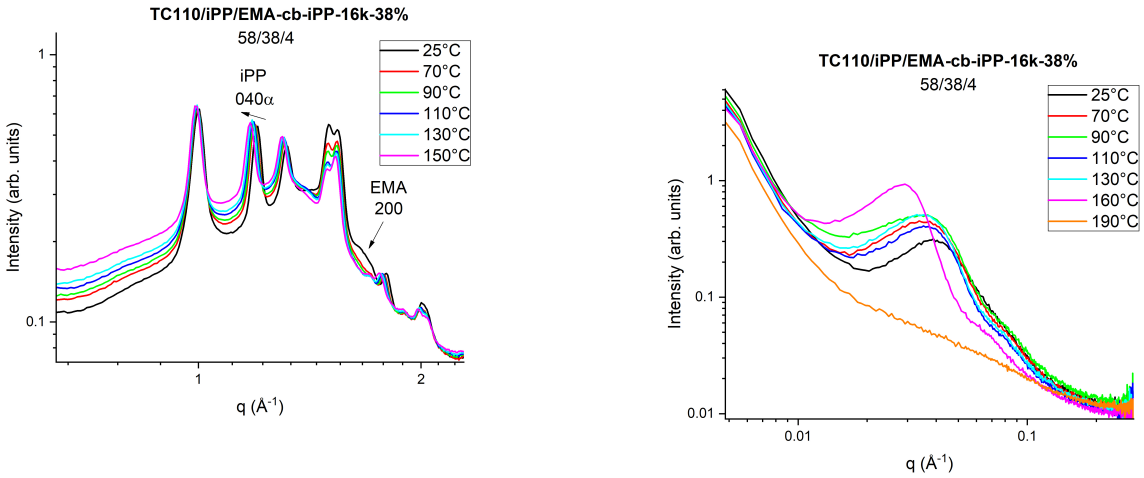

Figure S12. Temperature dependent WAXS (lhs) and SAXS (rhs) curves for the ternary blend. The WAXS shows loss of the 200 peak from EMA at elevated temperatures and this is attributed to melting of small EMA crystals in the compatibilized ternary blend. By 150-160 ºC, the EMA and the EMA-*cb*-iPP-16k-38 have melted; the minority iPP phase is not fully melted.

Section 9. AFM: Impact of temperature on EMA-cb-iPP morphology.

AFM images were collected using an Icon (Bruker, Santa Barbara CA). Images were collected in peak force QNM mode with pre-calibrated probes. Peak force QNM is a fast force curve imaging method where analysis occurs while imaging to extract relevant parameters of the sample and tip-sample interaction including the sample modulus (obtained by fitting the force curve to the DMT model) and tip indentation measurement, which are included in this study. RTESPA 300-125 (Bruker, 125 nm radius, spring constant of ~40N/m) cantilevers were used for imaging on the iPP/EMA blend. On the comb block sample, the room temperature measurement was conducted with an RTESPA 300-125 cantilever and all subsequent measurements above room temperature were conducted with an RTESPA 150-30 cantilever (Bruker, 30nm radius, spring constant of ~6N/m). Cantilevers were selected for a best match between the lever and sample mechanical properties for maximum sensitivity. All calibrations for peak force QNM and AFM-

nDMA were done on a reference sapphire sample. All samples were prepared by cryomicrotomy. Note that different areas of a given sample were imaged at each temperature.

Figure S13 shows a series of AFM logModulus images for the EMA/iPP homopolymer blend (40/60 wt/wt) at room temperature (10 μm x 5 μm, left), 100ºC (10 μm x 10 μm, middle), and 130 ºC (10 μm x 10 μm, right) where bright yellow regions represent higher modulus than the dark red/black regions. In these images, the stiffer iPP (yellow regions) can be easily differentiated from the softer EMA regions (dark red). These two phases are not miscible with one another as small (~100 nm wide) domains of EMA are observed. The elongated and thin domains of EMA within the iPP matrix indicate some degree of compatibility. As the temperature increases, the relative moduli between the two materials diverges, as observed in the modulus contrast. This we attribute to the full melting and consequently decreased modulus of the EMA phase in the 100 ºC and 130 ºC images. The relative compatibility appears to remain similar as a function of temperature.

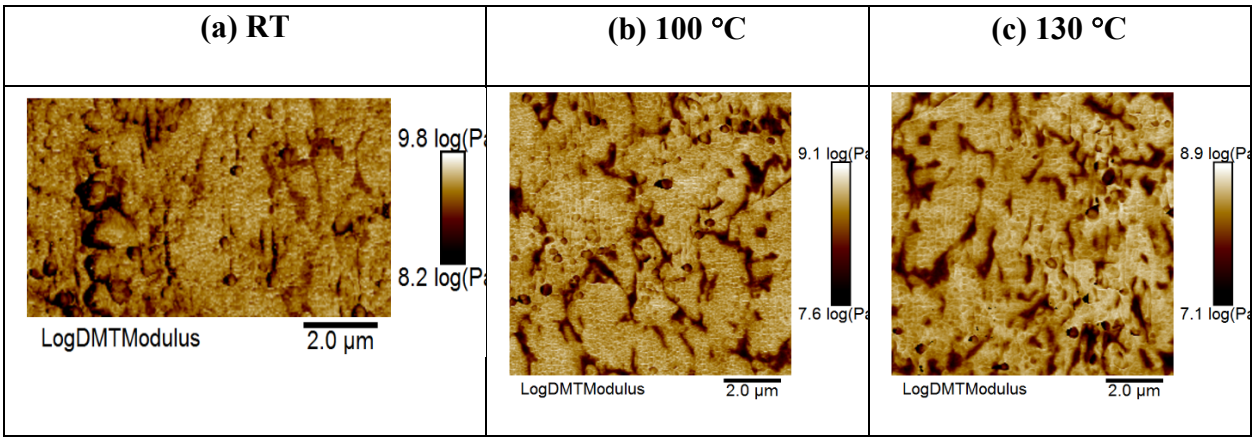

Figure S13: LogModulus AFM images of 40/60 EMA/iPP (unfunctionalized 2 MFR homopolymer) blend collected at (a) room temperature, (b) 100ºC and (c) 130ºC. In the figure, bright yellow regions represent higher modulus (assigned to iPP) than the dark red/black regions (assigned to EMA)

Figure S14 shows AFM images of EMA-cb-iPP-24% wt where the top images (fig S14a and S14b) were collected at room temperature and the bottom images (fig S14c and S14d) at 70°C. Fig S14a and S14b show peak force QNM images of a) log modulus and b) tip indentation into the sample. Note that the relative contrast between these two channels are inverted so that areas in the Log Modulus plot (S14a) that appear stiff (bright white/yellow contrast) will correlate with areas in the indentation plot (S14b) that show low (dark red/black contrast) indentation.

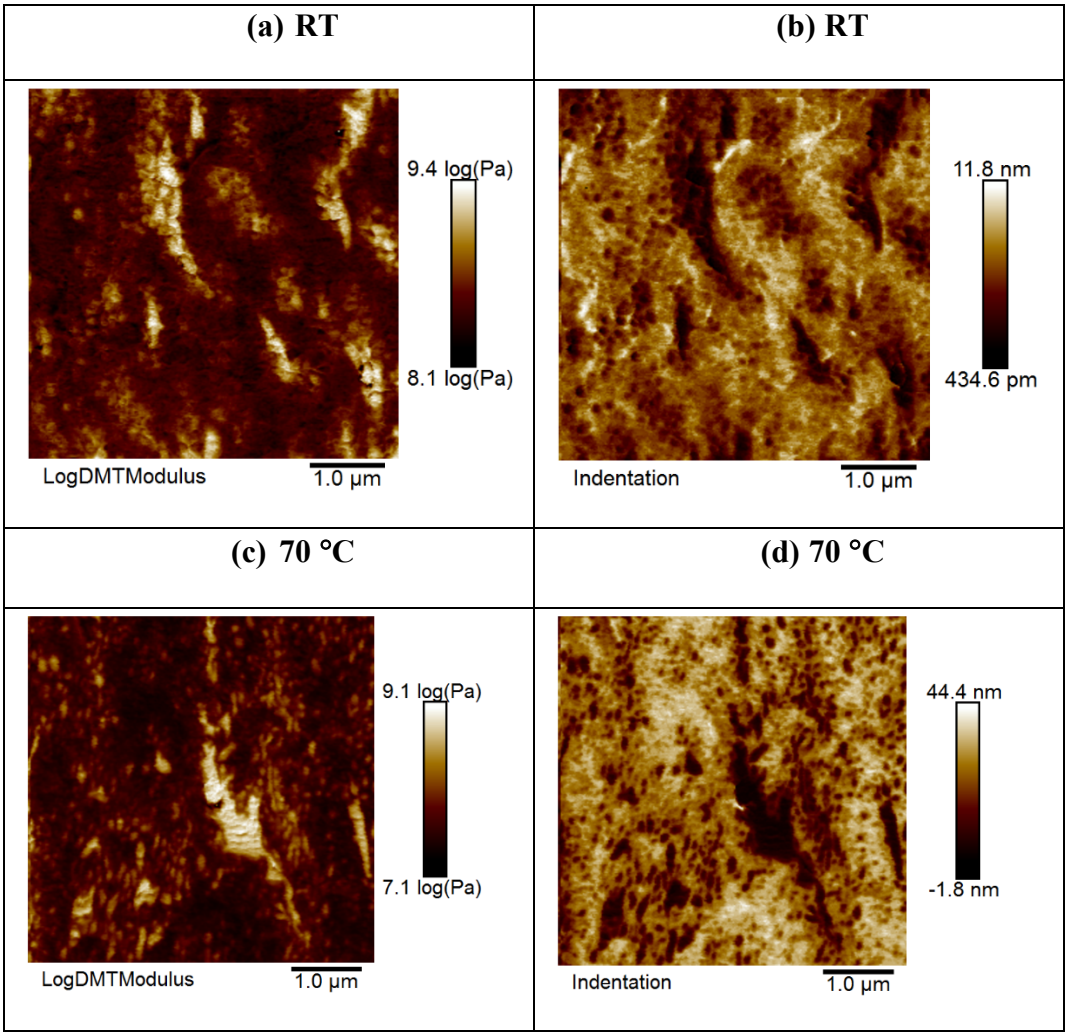

Figure S14: Log modulus (lhs) and indentation (rhs) AFM images of EMA-*cb*-iPP-16k-24 collected at room temperature and at 70 ºC. In the Log modulus images (a) and (c), higher modulus,

bright yellow regions are assigned to iPP, while lower modulus dark red/black regions are assigned to EMA. In the indentation images (b) and (d), the light yellow regions are assigned to EMA while the dark red regions, are assigned to iPP.

At room temperature, two phases – stiff and soft – are observed. The stiff component, assigned to iPP, is present as thin, elongated domains with a width of less than 100nm as well as small spheroidal domains of diameter 50-100nm, readily observed in the indentation image (Figure S14b). These features are comparable to those observed in the Cypher bimodal AFM and STEM images (Figures 7 and 8). At 70°C, lamellar structure within the stiff (iPP) domains is occasionally observed as in the central bright feature in Figure S14c.

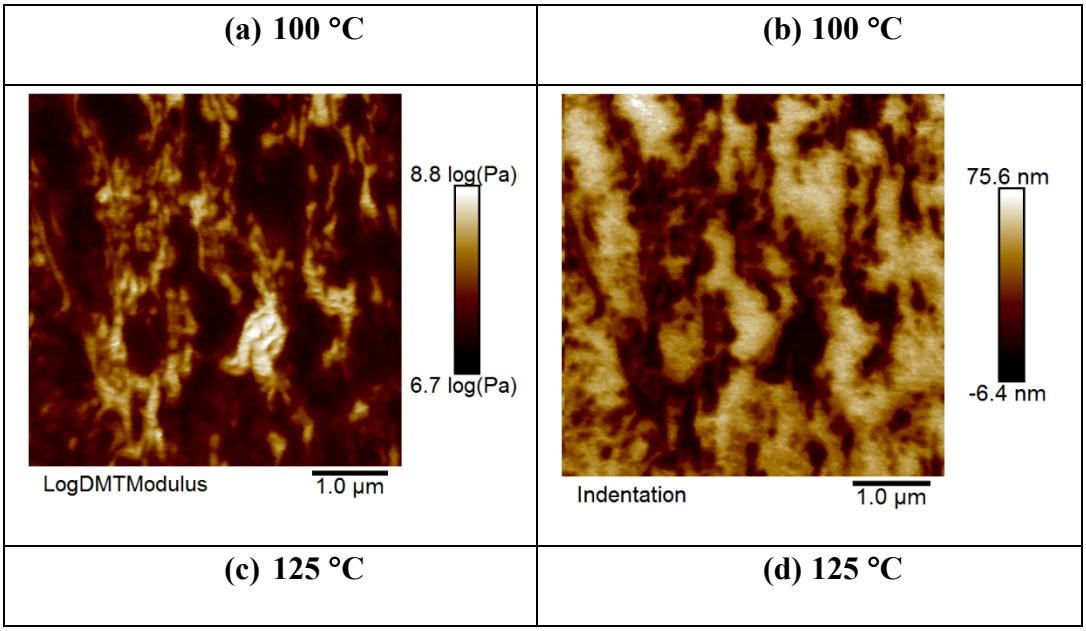

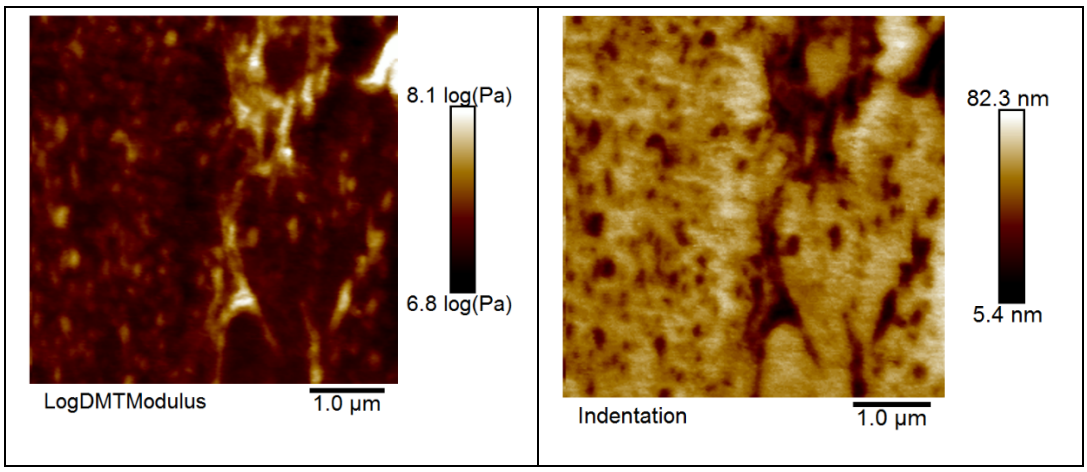

Figure S15: AFM images of EMA-*cb*-iPP-16k-24 collected at room temperature and at 100 °C (a,b) and 125 °C (c, d).

Log modulus and indentation images were collected for EMA-*cb*-iPP-16k-24 also at 100°C (Figure S15a and S15b) and 125°C (Figure S15c and S15d). The images at 100°C still show structure within the stiff (bright white in S15a) phase, as can be observed in the lamellar structure in the bright white features; again assigned to iPP. The softer area (dark in S15a) is featureless, where the lack of morphology can be easily observed in the corresponding indentation image (Figure S15b), corresponding to the onset of melting in this phase. This is consistent with full melting of the EMA at 100°C, a temperature still well below the melting peak (130°C) of the iPP. At 125°C, although both phases are still distinct, the stiff areas have now started to lose their morphology presumably with the partial melting of the iPP as well.

Finally, Figure S16 shows high resolution log modulus (S16a) and tip energy dissipation images (S16b) of the EMA-*cb*-iPP-16k-24 comb block at 100 °C. In the dissipation channel, 10 nm wide loops and other linear structures are observed, as marked by the red arrows. These structures appear to emanate from the soft phase (EMA) into the stiffer component (iPP).

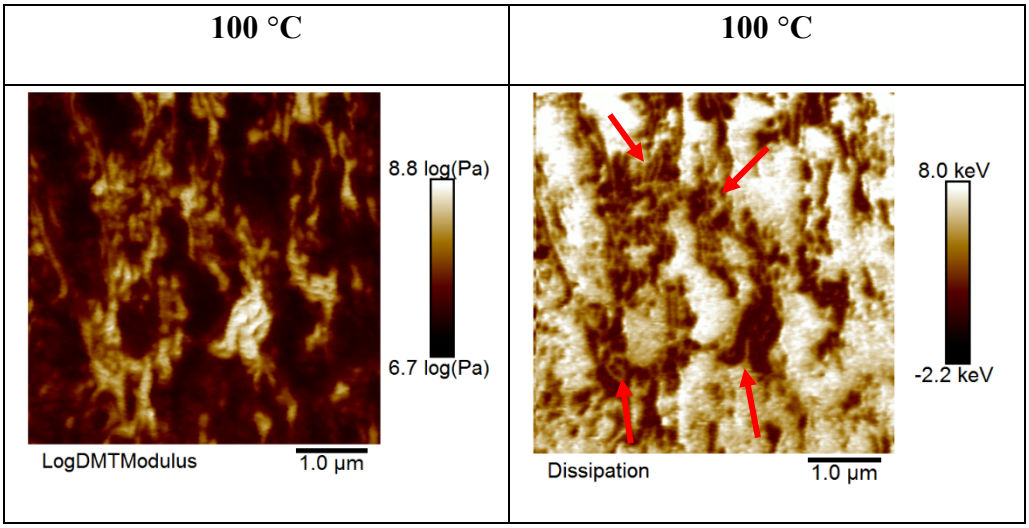

Figure S16: AFM micrographs of EMA-*cb*-iPP-16k-24 at 100 °C. Red arrows mark linear and loop shaped soft structures in the stiffer component (iPP, yellow in log modulus and dark red in dissipation).